



Minimum environmental load extension through compressed air extraction: Numerical analysis of a dry low NO_x combustor

Raditya Yudha Wiranegara^a, Uyioghosa Igie^{a,*}, Pierre Ghali^a, Kamal Abudu^a, David Abbott^a, Richard Hamilton^b

^a Centre for Propulsion and Thermal Power Engineering Cranfield University, Cranfield, Bedfordshire MK43 0AL, UK

^b Mitsubishi Power The Point, 37 North Wharf Road, London W2 1AF, UK

HIGHLIGHTS

- Combustor can handle minimum environmental load extension with airflow extraction.
- Up to 7% points load reduction is possible when translated in engine-level analysis.
- CO reduces by 12% with a necessary increase of fuel split ratio by 2%
- NO increases by 5% in relation to the peak values in normal operation at part-load.
- Combustor flame durability and stability do not appear to be significantly altered.

ABSTRACT

The operational flexibility of gas turbine (GT) engines is a key requirement to coexist alongside increasing renewable energy that is often intermittent. One of the GT flexibility criteria is the Minimum Environmental Load (MEL). This is the lowest load the engine can be operated, without infringing on emissions limits (particularly CO) and is relevant to periods when there is a priority to renewable generation or low power demand. This study along with a series of related works of the authors proposes compressor air extraction for MEL extension. Here, a stand-alone three-dimensional numerical dry low NO_x combustor demonstrates the technical viability concerning combustor performance and emissions. In addition, supplemented with low-order models for durability and stability evaluations. For the first time, there is evidence to show that the combustor can handle the 18% compressed air extraction to sustain a new MEL. This operation is characterised by a 12.3% reduction in CO through an increase of the fuel split ratio by 2% after design exploration cases. However, at the expense of a smaller overall rise in NO emissions by 5%. The durability analysis focused on the wall liner temperature assessments, which show no unusually high temperature rise for the new MEL. Similarly, the thermoacoustic instability frequencies and gains are around the normal operation mode. When benchmarked against previous related engine-level analysis, the evidence shows that the new MEL is a 7% points reduction of load.

1. Introduction

Environmental awareness has prompted a lot of policy changes on emissions in the power sector, especially in Europe. This has encouraged more adoption of renewable forms of power to mitigate carbon dioxide (CO₂) emissions connected to global warming. Nevertheless, renewable sources of power like wind and solar energy are intermittent and not on-demand. In addition, they do not directly offer the grid inertia that is required to provide stability on the electric grid [1]. One of the key advantages of gas turbine (GT) engines is a fast response to higher power output like 38 to 40 MW per minute [2,3]. Also, heavy-duty GT engines that are large rotating equipment drive synchronous generators. This coupling is such that the high momentum of their shaft serves as a

braking mechanism for the grid. This capability also extends to addressing momentary supply–demand imbalances. Hence GT currently provides the capability to back-up renewables in periods of uncontrolled low power generation or peak demand. This can ensure that the ability to increase renewable power is technically viable. When renewable power generation is high, some GTs on the electric grid is made to operate at low loads instead of a complete engine shutdown. The purpose of this is to avoid the thermo-mechanical stress that reduces the life of the engine for every start-up. Also maintaining the engine online at a low load ensures that the ramp-up to higher loads is shortened. While the engine is kept at a low load, a key combustion concern is the minimum environmental load (MEL). This is simply the lowest engine power output that can be attained without infringing emission limits, particularly the carbon monoxide (CO) emissions that tends to be dominant in

* Corresponding author.

E-mail address: u.igie@cranfield.ac.uk (U. Igie).

<https://doi.org/10.1016/j.apenergy.2023.120803>

Received 21 November 2022; Received in revised form 18 January 2023; Accepted 3 February 2023

Available online 17 February 2023

0306-2619/© 2023 The Author(s). Published by Elsevier Ltd. This is an open access article under the CC BY-NC-ND license (<http://creativecommons.org/licenses/by-nc-nd/4.0/>).

Nomenclature			
Abbreviations		T_{std}	Temperature standard deviation
BL	Baseload	u	Velocity
CC	Combined Cycle	x	Spatial direction
GT	Gas Turbine	Y	Mass fraction of species
PL	Part-Load	Greek Symbols	
ST	Steam Turbine	ε	Turbulence dissipation rate
BAT	Best Available Technique	ω	Angular Frequency
CFD	Computational Fluid Dynamics	μ	Viscosity
DPM	Discrete Phase Modelling	ϕ	Equivalence ratio
FAR	Fuel Air Ratio	ρ	Density
FGM	Flamelet Generated Manifold	∇	Gradient
FDF	Flame Describing Function	τ	Characteristic Time Delay
FDM	Finite Difference Method	σ	Turbulent Prandtl number
FSR	Fuel Split Ratio	ν	Volume of fluid
FTF	Flame Transfer Function	Letters and Symbols	
FSR	Fuel Split Ratio	\widetilde{c}^2	Reaction progress variance
OEM	Original Equipment Manufacturer	\widetilde{f}^2	Mixture fraction variance
MEL	Minimum Environmental Load	U^*	A function of mean strain, rotation rates and angular velocity
PDF	Probability Density Function	Headings	
RKE	Realisable $k-\varepsilon$ model	\sim	Mean part from scalar decomposition/ Density-weighted averaged
BREF	Reference Document	$\dot{\sim}$	Fluctuating part from scalar decomposition
CAES	Compressed Air Energy Storage	$-$	Non-weighted averaged
RANS	Reynolds-Averaged Navier Stokes	\sim	Vector
VIGV	Variable Inlet Guide Vane	Subscripts	
Letters		NO	NO (nitric oxide) species
c	Reaction progress	$pilot$	Part of pilot burner
D	Effective diffusion coefficient	$comb_inlet$	Part of combustor inlet
f	Mixture fraction	f	Flame-related parameter
k	Turbulence kinetic energy	$fuel$	Fuel-related parameter
M	Mach number	ref	Reference
n	Gain	$stoic$	Stoichiometric
p	Pressure	t	Turbulent
P	PDF		
q	Heat Release		
S	Source term		
t	Time		

this regime. CO peaks, resulting from incomplete combustion: when the amount of air to completely burn the fuel is relatively low. A comparatively lower MEL indicates a superior capability on low loads. The current state of the art from different original equipment manufacturers is shown in Abudu et al [4] which shows as low as 25 % MEL and high values of 75 %. These are all benchmarked to the CO limit referenced in the Best Available Technique (BAT) reference document for large combustion plants [5]. For GTs, the yearly average limit value is 50 mg/Nm³ for CO and 55 mg/Nm³ (in continuous operation).

Despite MEL being a key performance index of OEMs within operational flexibility, there is very limited research work in the open literature. By using CFD, Kulkarni et al. [6] numerically investigated MEL for a sequential combustor used in the GT24/GT26 engines. In this unique combustor design with two stages: EV combustor and SEV combustor, some of the burners in the latter are turned off to obtain low load and lower CO. By switching off some burners, more fuel is redirected to the remaining burners, increasing flame temperature that promotes more CO burnout. A related study for the same combustor indicates that the MEL of 20 % for the standalone GT [7] and also referred to in Kulkarni et al. [6]. This value is not demonstrated in the numerical study as it focuses only on the combustor performance. More specifically it is a large eddy simulation study of the SEV performance, showing low CO emissions at low part load operations. It was found that not only can the

MEL be lowered, but the CO emissions are also reduced below the legal limit [78]. The same concept has also been tested on an annular EV combustor of the differences shown in Magni et al. [8]. RANS-CFD simulation was employed to study the difference in the temperature profile between the baseload, part-load without burner switched off and part-load with burner switched off. The work showed a higher local hot spot temperature in the part load with the burner switched off. Nevertheless, the temperature is still acceptable for turbine operating conditions. In addition, the work also included extended VIGV closure, which was set down to -45° . It is claimed that the combination of the concept and the latter manages to reduce the MEL to 26 % GT load with an improvement in fuel savings by 17 %.

The authors present an operational concept for load reduction through air extraction after the compressor (before the combustor inlet) in papers [9,10]. This load turndown is achieved by storing the pressurised air in a compressed air energy storage (CAES) application. In the same project (TURBO-REFLEX) and for the first time, the authors proposed a combination of air extraction, variable inlet guide vane (VIGV) closure and subsequent drop in the combustor temperatures to improve the MEL as presented in Abudu et al. [4]. This novel approach described in the referred paper results in a reduced MEL of 31 % of the power output compared to the 47 % design value. This 34 % reduction in the MEL was achieved with 24 % air extraction, also using the CO emissions

standard limit mentioned. However, the CO emissions predicted in the study were obtained from a generalised correlation rather than a combustor-specific simulation/experimental work. Further details of this engine-level operational regime using a low-fidelity model are included in [Figures A1 and A2 of the Appendix](#). In advancing our work further, high-fidelity modelling of the standalone compressor under air extraction and VIGV closure was conducted by Szymanski et al. [10]. This showed that the compressor under such operation can only allow for up to 18 % of air extraction due to choking and high flow separation. Consequently, this updated extraction limit is a more conservative prediction than in the earlier study. The update is crucial, given that the allowable limit of air extractions or MEL extension needs to be compliant for the major components including the combustor, hence the rationale for the present study.

For the first time, the technical viability of high air extraction to the inlet of the GT combustor is numerically assessed. The investigation was carried out employing the 3D RANS-CFD simulation in the introductory and validation paper of the model presented in Wiranegara et al. [11]. More specifically on the combustor behaviour with extended MEL, the work here is to substantiate:

- the combustor performance at the extended MEL in terms of efficiency and emissions (NO and CO)
- the thermoacoustic instability of the combustor in this new MEL, compared to normal operations (baseload and part-load)
- the liner wall temperature distribution used at extended MEL, as a way to evaluate the durability
- the most favourable pilot and main burner fuel split that leads to a more emissions-compliant operation.

2. Combustor model

The combustor model developed is of DLN design, incorporating Mitsubishi-type technology. It comprises the burner region, the basket/chamber section and a transition piece, as shown in [Fig. 1](#). The burner section consists of main burners surrounding a single pilot burner at the centre of the arrangement. Cooling is incorporated into the combustor chamber and transition piece. At part load, by-pass air is fed into the transition piece from the compressor discharge casing. This allows the flame temperature to be maintained at a higher value as the load and thus turbine inlet temperature is reduced. To reduce the computational time, only a quarter section of the 3D model is used. [Fig. 2](#) shows the quarter model, the domains along with locations for the specification of boundary conditions. These locations consist of the combustor inlet, fuel inlets, cooling inlets at the combustor chamber and transition piece, combustor outlet and solid walls. An inset in the figure shows an enlarged view of the main and pilot burners, highlighting the fuel inlets. Air pressure and temperature are defined at the combustor inlet. Air mass flow rate and temperature are defined at the combustor chamber and transition piece cooling inlets, with the temperature set to be the

same as the inlet. At part load, the air mass flow rate is defined at the bypass valve inlet. This flow is scheduled based on the GT operation and required power output. The flow parameters specified at the fuel inlets are fuel mass flow rate and temperature. Also, the flow rate split between the pilot and main burners varies and is scheduled based on the engine power output. The chemical kinetics involved in the combustion of methane, used as fuel, is described by the GRIMech 3.0 mechanism [12]. At the combustor outlet, a target is set for the mass flow rate and with this being specified, the outlet pressure is adjusted at every iteration until it meets the required mass flow rate.

[Table 1](#) shows the boundary conditions for full load (baseload - BL), part-load (PL) and design MEL and cases of extended (Ex) MEL for various airflow extractions signified by the % mass flow amount. Most of these engine boundary conditions have been obtained from Abudu et al [4], in the directly related study using Cranfield's in-house code: TURBOMATCH [12]. The bypass valve scheduling was also obtained from the dataset in the aforementioned reference, while the fuel split ratio between the main and pilot and its scheduling against load have been adapted from Tanaka et al. [13]. Given the work of Szymanski et al [10] up to 18 % of air extraction is studied here for the Ex.MEL cases as the maximum allowable extraction rate. In addition, a 15 % air extraction case is performed to represent a less aggressive reduction.

3. Methodology

The methodology of the combustor modelling for performance and emissions, thermoacoustics (stability) and durability (via liner wall heat transfer evaluations) is described in this section.

3.1. Modelling – Turbulence, Flame and emissions

The modelling involves the use of Reynolds-Averaged Navier-Stokes (RANS) equations, with an improved $k - \epsilon$ model known as the realisable $k - \epsilon$ (RKE), as shown in [Equation \(1\) and Equation \(2\)](#). The RKE has been used widely in most RANS combustion studies [14–18]. The term 'realisable' emphasises the capability in working around some mathematical constraints imposed by the Reynolds stresses, which gives the advantage to be consistent with turbulent flow physics. Further details of the RKE formulation can be found in [19] that in addition shows that the constant, C_{μ} , found in the turbulent viscosity, μ_t , formulation is no longer a constant value, 0.09. Instead, it is a function of local mean flow deformation. Another characteristic of the model is the modified transport equation for the turbulent dissipation, usually marked ϵ^* . To enable representation of the turbulent vortex shedding and dissipation terms, the equation is derived from the dynamic equation of fluctuating vorticity; hence, omitting the production terms for turbulent kinetic energy, k .

k -equation:

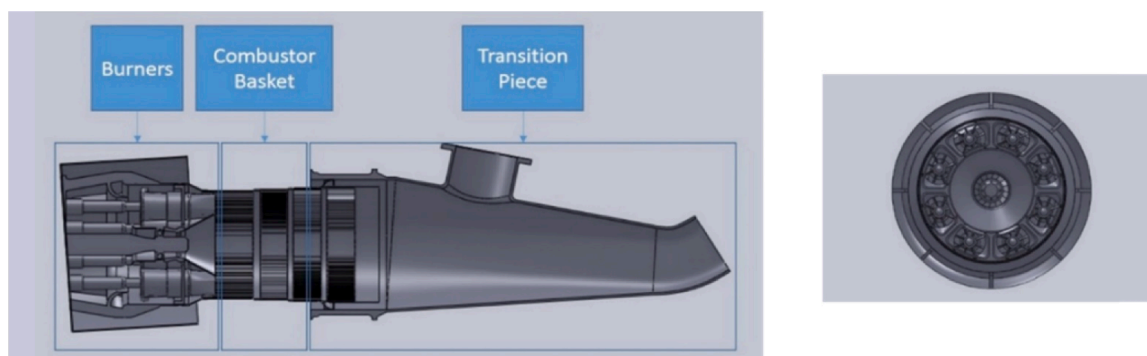


Fig. 1. 3D combustor model [11].

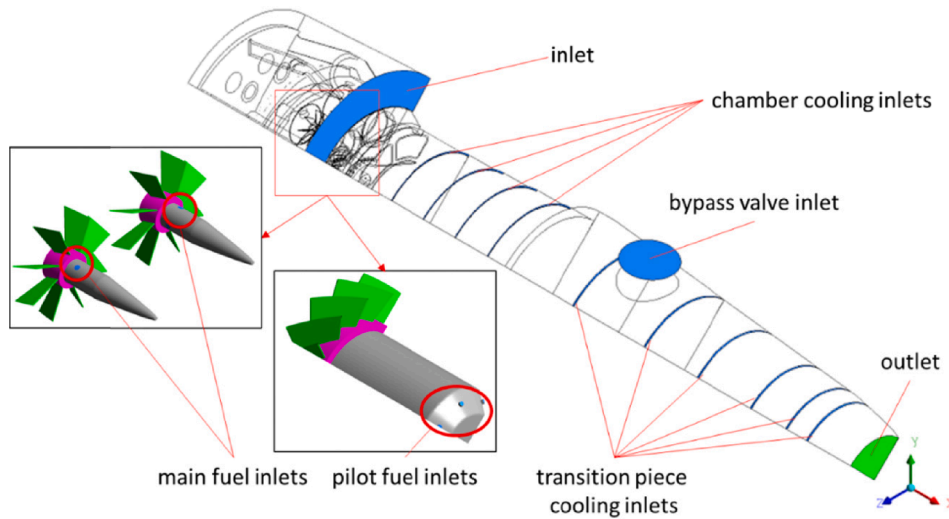


Fig. 2. Boundary definitions on the quarter-section of the model.

Table 1
Boundary conditions of the BL, PL, MEL and Ex.MEL cases [4].

Parameters	BL	PL	MEL	Ex.MEL (15 %)	Ex. MEL (18 %)
GT load (%)	100	68	47	45	40
Inlet air pressure (bar)	15.9	12.24	11.17	10.37	10.01
Inlet air temperature (K)	692	654	638	621	616
Combustor inlet mass flow rate (kg/s)	23.5	18.4	18.4	15.6	15.1
Bypass valve flow (% of air inlet)	0	8.72	14.21	14.97	16.19
Fuel Temperature, K	413				
Global Equivalence ratio, Φ	0.53	0.50	0.37	0.48	0.47
Pilot Equivalence ratio, Φ_{pilot}	0.56	1.33	1.12	1.52	1.65
Main Equivalence ratio, Φ_{main}	0.61	0.58	0.45	0.58	0.58

$$\rho \frac{\partial k}{\partial t} + \frac{\partial}{\partial x_j} k u_j \rho = \frac{\partial}{\partial x_j} \left[\left(\mu + \frac{\mu_t}{\sigma_k} \right) \frac{\partial k}{\partial x_j} \right] + \mu_t S^2 - \rho \epsilon - 2\rho \epsilon M_t^2 \quad (1)$$

ϵ^* -equation:

$$\rho \frac{\partial \epsilon^*}{\partial t} + \frac{\partial}{\partial x_j} \epsilon^* u_j \rho = \frac{\partial}{\partial x_j} \left[\left(\mu + \frac{\mu_t}{\sigma_{\epsilon^*}} \right) \frac{\partial \epsilon^*}{\partial x_j} \right] + \rho C_1 S \epsilon^* - 1.9 \rho \frac{\epsilon^*}{k + \sqrt{\nu \epsilon^*}} \quad (2)$$

$$\sigma_{\epsilon^*} = 1.2, C_1 = \max \left[0.43, \frac{\eta}{\eta + 5} \right], \eta = S \frac{k}{\epsilon^*}, S = \sqrt{2S_{ij}S_{ij}}$$

Also, a partial-premixed combustion model is employed in this study, using the Flamelet Generated Manifold (FGM) model [20]. Based on the flamelet theory, the assumption is that a multi-dimensional turbulent flame is an ensemble of one-dimensional laminar flames where all thermochemical scalars are embedded within each flame from which a manifold or a database is constructed. The database is mainly controlled by two scalar variables, namely mixture fraction (f) and reaction progress (c). In addition, the variance of each control variable, i.e. \tilde{f}^2 and \tilde{c}^2 , is required in the function. The values of these variables are obtained by solving each variable's transport in Equation (3) and Equation (4) presented in the form of density-weighted average. A function is required to describe the statistical distribution of these control variables, which fluctuate due to turbulence. Hence, a joint Probability Density Function (PDF), $P(c, f)$ is acquired. The details of this calculation provided in the previous work of the authors [11]. In this work, the shape of the joint PDF is described using the assumed β -function. A closure is

required for the reaction progress source term, S_c , which describes the physio-chemistry interaction between the turbulence and chemical reaction of the species involved. This work employed a model that describes the wrinkling and thickening of the flame front developed by Zimont [21]. The model considers the varying degree of turbulence eddy scale influences on laminar flamelet [22]. Similarly, previous works of the authors [11] give details of equations and outline the considerations that the model must cover.

\tilde{f} -equation:

$$\frac{\partial \rho \tilde{f}}{\partial t} + \frac{\partial}{\partial x_i} (\tilde{f} \tilde{u}_i \rho) = \frac{\partial}{\partial x_j} \left[\left(\frac{k}{C_p} + \frac{\mu_t}{\sigma_k} \right) \frac{\partial \tilde{f}}{\partial x_j} \right], \quad (3)$$

\tilde{c} -equation:

$$\frac{\partial \rho \tilde{c}}{\partial t} + \frac{\partial}{\partial x_i} (\tilde{c} \tilde{u}_i \rho) = \frac{\partial}{\partial x_j} \left[\left(\frac{k}{C_p} + \frac{\mu_t}{S_{c_i}} \right) \frac{\partial \tilde{c}}{\partial x_j} \right] + \rho S_c \quad (4)$$

Where C_p is the heat capacity at constant pressure, S_{c_i} is the Schmidt number for turbulent flow and S_c is the source term for the reaction progress.

For NOx emission which is mainly comprised of nitric oxide (NO), it has been the focus. The NO calculation is decoupled from the FGM due to its relatively slower chemical timescale than the turbulent time scale. It is approached as post-processing after convergence; this is by solving a separate transport equation for the NO mass fraction (Y_{NO}) that is acquired and expressed in Equation (5) as

$$\rho \frac{\partial \tilde{Y}_{NO}}{\partial t} + \frac{\partial}{\partial x_i} \tilde{Y}_{NO} \tilde{u}_i \rho = \frac{\partial}{\partial x_j} \left[\rho D \frac{\partial \tilde{Y}_{NO}}{\partial x_j} \right] + S_{NO} \quad (5)$$

Where \tilde{Y}_{NO} is the mass fractions of NO and D is the effective diffusion coefficient. Each formation pathway constitutes a different definition of the NO reaction source term, S_{NO} . Wiranegara et al. [11] present the equation for the mean of the NO reaction source term, given that the turbulence effect influences the flame, thus the formation of NO. The use of PDF has also been employed using the using β -function.

The computational mesh shown in Fig. 3 and further details of the modelling are presented by Wiranegara et al. [11] which shows the mesh and independence study, together with the verification of the model when compared to the experiment study reported by Ruan et al [23]. Wiranegara et al. [11], considers three mesh cases (6.3, 10.6, and 23.1 million nodes), justifying that the 10.6 million node case is appropriate. The RKE model requires a y^+ above 30 in the inner layer of the log-law region because it employs a standard wall function to

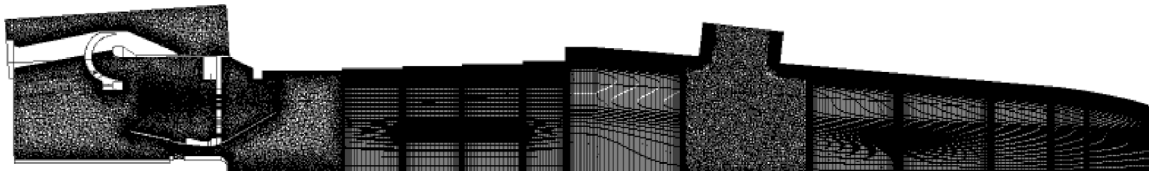


Fig. 3. Computational mesh of the quarter-model [11].

capture the near-wall physics hence, a y^+ of 30 was used. A non-slip boundary is defined on the solid walls which are assumed to have an emissivity of 0.7. The validation of the model was first presented in Wiranegara et al. [11] and is discussed further in Section 3.4.

3.2. Durability analysis (via wall liner Evaluation)

As wall temperature has a significant impact on durability, a change in predicted wall temperature was taken as an indicator of the impact of changes in operation on durability. Another key factor in combustor component life is the thermoacoustic behaviour of the combustion system and this is considered separately in subsection 3.3. This was of particular importance for the Ex. cases, to substantiate if the new type of operation is technically viable. To investigate this, a Cranfield in-house code was used to evaluate the liner wall temperature distribution. It calculates heat transfer between the hot gas and the liner wall using the Finite Difference Method (FDM) developed in MATLAB [24].

The FDM heat transfer analysis considers the cooling geometry of a combined cooling system that incorporates impingement and effusion cooling methods. Correlations are employed in the code to calculate the coolant thermodynamic properties, such as the specific heat capacity, heat conductivity, and viscosity. The specific heat capacity is computed using a curve-fitted polynomial expression provided in [25]. On the inner side of the wall, the combustion zonal temperature was extracted from the CFD simulation. The liner wall considered in this code has a double-wall arrangement shown on page 11 of the reference [24], where the coolant flows within the wall enclosure before then joining in the main combustion flow. The domain of interest in the code is limited to the element on the inner liner wall adjacent to the hot combustion gas. Based on the conservation of energy, the heat balance within the domain of interest is expressed as:

$$(R_1 + C_1)\Delta A_{w1} - C_1 A_{hs} = (R_2 + C_2)\Delta A_{w2} = K_{1-2}\Delta A_{w1} \quad (6)$$

Where K_{1-2} is the conductivity through the liner wall, R_1, R_2 are the radiation at the internal (1: hot gas side) and external (2: coolant side), ΔA_{hs} is the effusion hole surface, $\Delta A_{w1}, \Delta A_{w2}$ are the elements on the internal and external surfaces, C_1 is the internal convection and C_2 is the enhanced convection due to impingement cooling on the element of the external surface, ΔA_{w2} . Semi-empirical correlations are employed to calculate the convection that accounts for the cooling effectiveness of the effusion cooling and the effect of impingement cooling. Details can be found in Y. Liu et al. [24] alongside Fig. 4. This figure shows an element, as indicated by the red arrow, within the hot side of the liner wall that has been discretised in nodal points and elements in the x and y directions. The element has been subjected to conduction on its upper, left and right sides, while on the bottom side, it is radiation and convection. Based on these descriptions, Equation (6) can then be rewritten as:

$$(R_1 + C_1)\Delta A_{w1} = K_{1-2}\Delta A_{w1} \quad (7)$$

With the heat balance defined at the centre node (j, k) , Equation (7) can then be rewritten in its discretised form as:

$$\begin{aligned} -k\Delta x \frac{T_{j,k} - T_{j,k+1}}{\Delta y} - k \frac{\Delta y(T_{j,k} - T_{j-1,k})}{2\Delta x} - k \frac{\Delta y(T_{j,k} - T_{j+1,k})}{2\Delta y} \\ = h\Delta x(T_{j,k} - T_c) + 0.5\sigma_0(1 + \epsilon_w)\epsilon_g T_g^{1.5} (T_g^{2.5} - T_{j,k}^{2.5}) \end{aligned} \quad (8)$$

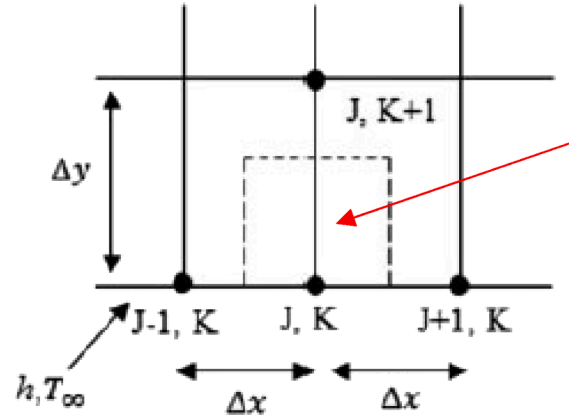


Fig. 4. An element within the hot side of the liner wall [24].

Where k is thermal conductivity, h is the heat transfer coefficient, ϵ_g, ϵ_w are the emissivity of the hot gas and liner wall, σ is the Stefan-Boltzman constant, T_c, T_g are the temperature of the coolant and hot gas.

Incorporating this stand-alone heat transfer model into the CFD involved extracting parameters such as the air mass flow rate distribution (for the cooling and combustion), hot gas mass flow rate, cooling geometry and equivalence ratio of the hot gas. To achieve this, the CFD computational domain was grouped into 12 segments as shown in Fig. 5. This segmenting was based on the location of the cooling outlets indicated in Fig. 2. In addition, the mentioned parameters extracted are in relation to each of the segments. Parameters, such as the air and hot gas mass flow rates, were axially averaged across each segment. Hence, each segment is represented by a single value of each parameter applied in the stand-alone thermal analysis code. The calculation was individually performed at each segment, resulting in the liner wall temperature distribution subsequently applied in the CFD model. It is important to state that for the initial CFD calculation, a value of 1000 K was used across the wall liner temperature, particularly in the vicinity of the combustion zone. The use of the two-dimensional heat transfer model ensured that the temperature variation expected in an actual combustor is accounted for in the final CFD model.

3.3. Thermoacoustic – Flame stability

The stability of the combustor flame for all conditions of interest has been investigated using a low-order acoustic network model. The approach considers decoupling the calculations into a series of acoustic networks and perturbed flame response [26]. In this approach, the combustor geometry is assumed to be a series of simple geometric elements described by acoustic transfer matrices. The perturbed flame response due to the acoustic disturbances can be characterised either by a Flame Transfer Function (FTF) [27] for a linear analysis or a Flame Describing Function (FDF) [28] for a non-linear analysis. The approach is different from the direct numerical calculation using time-varying CFD, in which the acoustic oscillation is coupled with fluctuating heat release from the combustion flame. The approach was not considered here due to the high computational demand in modelling the fluctuation which requires scale-resolving CFD approaches, such as LES or DNS.

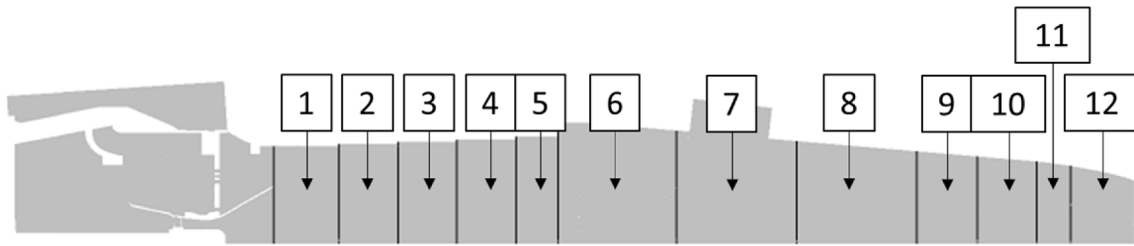


Fig. 5. Segments for the heat transfer analysis.

This approach is extremely computationally demanding and was not considered appropriate for this study. The network model used in this investigation is the open-source code OSCILOS [26] and the version used for this study is OSCILOS_long, which considers only the longitudinal modes. This is appropriate for the cylindrical can-based combustor in this study as longitudinal modes dominate, particularly at low frequencies [26].

The combustor has been simplified into a series of cylinders, as shown in Fig. 6. Also, the thermodynamic conditions at the inlet must be defined in the code to calculate the velocity and temperature profiles. The conditions were obtained from the inlet boundary conditions defined in the CFD simulation. Thermal and flow properties of the flame in the thermoacoustic model are determined by the equivalence ratio in the CFD simulation. As shown in Fig. 2, the main and pilot burners are arranged in parallel. However, in the thermoacoustic code, they have to be in series due to the dimensionality of the code. As a result, it is necessary to recalculate both flame equivalence ratios to achieve a similar temperature rise as in the CFD simulation. These are expressed as:

$$Flame1FAR, FAR_{f1} = \frac{\left(\frac{W_{fuel} \times FSR}{1 + FSR}\right)}{W_{comb_inlet}} \quad (9)$$

$$Flame1\phi, \phi_{f1} = \frac{FAR_{f1}}{FAR_{stoic}} \quad (10)$$

$$Flame2FAR, FAR_{f2} = \frac{\left(\frac{W_{fuel}}{1 + FSR}\right)}{W_{comb_inlet}} \quad (11)$$

$$Flame2\phi, \phi_{f2} = \frac{FAR_{f2}}{FAR_{stoic}} \quad (12)$$

Where FSR is the fuel split ratio between the main and pilot burners. In this work, the flame response would be characterised by the Flame Transfer Function (FTF) expressed as:

$$FTF(\omega) = \frac{\hat{q}/\bar{q}}{\hat{u}_{ref}/\bar{u}_{ref}} \quad (13)$$

Where ω is the angular frequency.

Equation (13) highlights the general relationship between acoustic oscillation and fluctuating heat release. The normalised velocity

oscillation, $(\hat{u}_{ref}/\bar{u}_{ref})$ at a location upstream of the flame (e.g. immediately upstream of the injection holes) and normalised fluctuating heat release (\hat{q}/\bar{q}) represent each component in the equation. The \hat{a} and \bar{a} signs indicate fluctuating and the mean parameters respectively.

The FTF can be determined in some ways: experimentally, numerically or analytically. Experimental data is not available for this system and non-standard operating conditions are being investigated. This study uses RANS CFD as its principle tool and thus only steady-state information is available. To determine the FTF an analytical model relating steady-state information to the acoustic (time-varying) characteristics of the flame is needed. The first such model (the $n-\tau$ model) was proposed by Crocco [27] which relates the FTF to a characteristic time delay (τ) as follows:

$$FTF(\omega) = ne^{-i\omega\tau} \quad (14)$$

Where n is the gain that represents the magnitude of the interaction between acoustic oscillation and heat release fluctuations and τ is the characteristic time representing the time delay between the initial perturbation and the heat release fluctuation. This standard $n-\tau$ model is available in OSCILOS and was chosen for this study. This model requires two constants to be evaluated, n and τ .

It can be seen from Equation (14) that n is not a function of ω , thus the low-frequency limit of n applies to all frequencies. It is often assumed that this low-frequency limit is $n = 1$. This assumption is strictly true for fully premixed combustion where pressure and flow perturbations in the vicinity of the burner cannot modify the equivalence ratio at the flame [29]. This is a reasonable approximation for this work which considers premixed combustion, however, it is recognized that some air-fuel ratio fluctuations may occur.

To determine τ , this work employs an approach that virtually injects tracking particles from the fuel injection holes to the flame front as suggested by Lieuwen et al. [30]. In the CFD simulation, this was determined by using the Discrete Phase Model (DPM) of ANSYS FLUENT. A band of lightweight and small particles are injected from the fuel holes, in this case, of the main and pilot burners. The mass flow rate has been set to be in the order of 10^{-10} not to affect the simulation. A surface representing the flame surface is marked for the particle residence time measurements. An isovalue of reaction progress of 0.9 was chosen to represent the flame location at which the majority of the combustion has been completed. In practice, this was defined in the

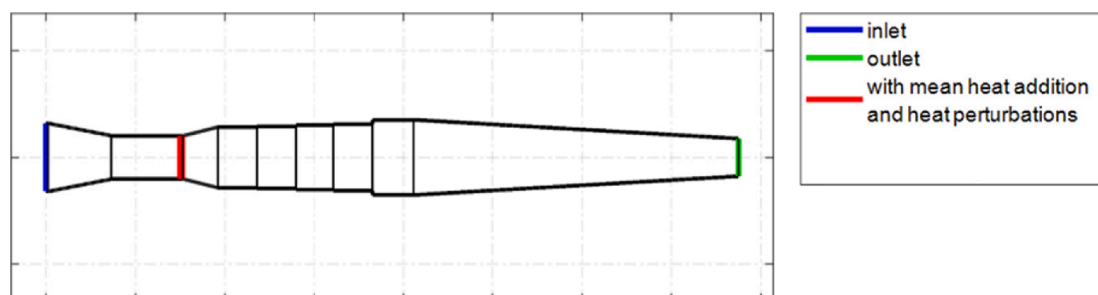


Fig. 6. Developed combustor geometry for the analysis in OSCILOS.

range of ± 0.01 of the actual isovalue, which gives 0.89 and 0.91.

The range provides an adequate layer of the flame front, to ensure the surface boundary captures all injected particles. The characteristic time delay for both the pilot flame and the main flame was determined by evaluating the mean time from fuel particle injection to particle interaction in this isosurface.

3.4. Validation

The validation of this modelling approach is provided in the previous work of the authors [11] which compares the results of this CFD combustor with a Mitsubishi experimental burner [23] under the same conditions. The results are also presented in Figures A3 and A4 in the Appendix of the present paper. It shows radial profiles of temperature, and mass fractions of CO₂, CO and NO at two axial planes with reference to the basket inlet of the burner. From these results, it can be observed that the predictions generally match closer with more axial distance (plane B) away from the burner outlet and suggests that the model predicts the flame stabilises further upstream than the experimental results. However, the form of the profiles is captured. For plane B which is 0.087 m from plane A, the maximum percentage errors are 3 %, 13 %, 73 % and 45 % for temperature, mass fractions of CO₂, CO and NO respectively.

4. Minimum Environmental load (MEL)

The MEL of the 3D combustor is presented here, based on the engine power settings explained in Abudu et al. [4] and provided in Table 1. This operation is at 47 % of power output with the corresponding boundary conditions obtained from the engine model shown in the table. Turndown from baseload to the design MEL is achieved in two main phases. In the first phase, the VIGV is progressively closed while maintaining a constant turbine entry temperature (TET). In the second phase, the TET is reduced until the CO limit of 40.5 ppmv is reached. This CO limit defines the MEL and is based on the BAT reference document for large combustion plants [5]. It is important to state that the first phase of the operation would normally result in a rise in the exhaust gas temperature. However, this isn't the case in this engine model which incorporates by-pass air, that is also featured in the 3D CFD transition piece used here. The chosen PL operating point is 67 % of the load and the end of phase one, where there is a maximum closure of the VIGV at constant TET. As such, the power output at PL is greater than MEL. This PL operation has been included in this analysis as it was identified to produce the local peak NO and temperature. Hence, used for reference in normalising the data. For CO, the BL (100 % load) shows the local peak values and is hence used as a reference to normalise the CO data.

Fig. 7 shows the mass-average axial profile of the normalised CO and NO concentrations, also temperature for BL, PL and MEL operations. The

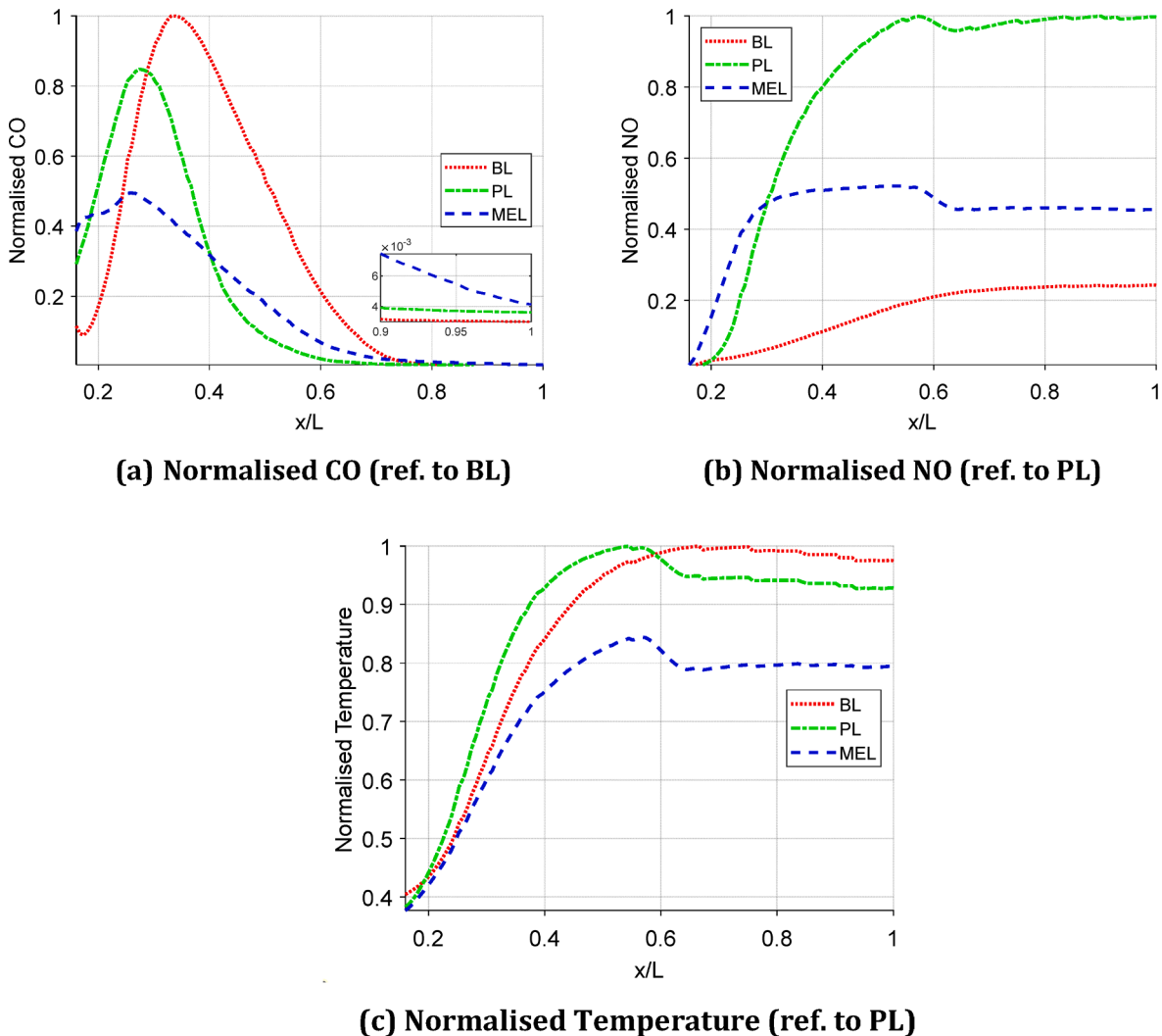


Fig. 7. Mass-average axial profiles of normalised parameters at BL, PL and MEL.

plot range is limited from the burner outlet at $x/L = 0.16$ up to the combustor outlet at $x/L = 1$. The evolution of the CO for all operations is shown in Fig. 7a which indicates that from the burner outlet, the CO begins to initially increase. This increase is a result of the combustion of early-stage fuel mixing which persists to peak values and is followed by gradual continuous reductions. Dilution due to the bypass air used in the PL and MEL cases is seen in the NO and temperature results at $x/L \sim 0.6$. This dilution also occurs in the CO results but is not apparent due to the low levels of CO at this axial location. The NO and temperature trends are generally similar to each other. PL has the fastest rise to the peak value of temperature ($x/L = 0.55$), however, the temperature is reduced subsequently because of the bypass air into the transition piece. The MEL case has an identical trend but with lower temperatures. It is also evident to see that the transition piece bypass air for cooling is also in use, as the drop in temperature at $x/L = 0.64$ coincides with the same location for the PL temperature drop. MEL has a lower average operating temperature than PL, resulting from a lower pilot equivalence ratio and global equivalence ratio. At BL no bypass air is injected and it can be seen that high temperatures are maintained up to the exit of the combustor outlet with only a small reduction from the peak due to cooling air ingress. Despite the higher temperature, BL operation demonstrates the lowest NO at the combustor exit. This is directly related to operating the lowest pilot equivalence ratio shown in Table 1. This contrasts with PL which operates at the highest pilot equivalence ratio among these three cases, and gives the highest NO at the combustor exit. This is due to the dominance of the diffusion pilot in the NO generation. The common trend in gas turbine operation, particularly with lean premixed, shows that at a lower load, the NOx emissions are lower than its BL, with the CO emissions exhibiting the opposite [31,32]. However, in this study, it is not the case, due to the inclusion of a pilot burner that helps to additionally stabilise the flame. Therefore, not a fully pre-mixed burner.

At the exit of the combustor, the emissions and temperatures are compared relatively and presented in Table 2. In the table, the ratio above 1 means the corresponding operating condition is higher than the BL. This applies to the CO and NO, for both PL and MEL. For the exit temperatures, these two part load temperatures are lower than the BL case. As expected, the MEL demonstrably shows the highest CO, due to incomplete combustion (also related to the lowest global fuel-to-air ratio). The MEL case operates with about 0.75 times less fuel than the PL operation.

Fig. 8 adds more insights into the emissions from the perspective of the fuel left over at $x/L = 0.9$, which is close to the combustor outlet. The maximum CO values for the MEL were used to normalise the concentration shown for all the conditions. The BL case shows the least CO concentration, followed by the PL case. For the PL operation, a region of low CO concentration at the combustor central region is observed. This may be attributed to the influence of the bypass-valve air flow that acts as additional air entrainment inducing local quenching. In the MEL case, a lower fuel rate causes the reduction of the combustion primary zone temperature, which eventually leads to higher CO concentration than in the other conditions. The contour plot of the CH_4 mass fraction shows fuel left over in the MEL case related to incomplete combustion.

5. Extended minimum Environmental load (Ex.MEL)

Reducing the MEL to lower loads without compromising CO offers advantages in terms of the reduced amount of fuel burn, and the ability to still provide inertia to the grid as the engine is still online. Also, it

Table 2

PL and MEL emissions and temperature ratios ref. to the BL.

Operating Conditions	CO/CO_{BL}	NO/NO_{BL}	T/T_{BL}
PL	1.20	4.11	0.95
MEL	1.38	1.88	0.81

ensures that the ramp-up of the engine is from a low load rather than a complete start-up that introduces delays. This section of the paper presents the implications of the extended MEL (Ex.MEL) caused by compressed air extraction before the combustor. Like the previous section, the approach to achieving this is introduced and described by Abudu et al. [4]. As with the MEL case, there are two phases. The first is a closure of the VIGV and maintaining a constant TET. The second phase is air extraction at the compressor outlet, while still maintaining the TET throughout, to deliberately mitigate the rise in CO. Unlike the referred work that provides additional high extractions, the limits have now been curtailed to Ext 18 % based on high-fidelity modelling of the compressor aerodynamic limits [10] discussed in Section 2 of the present paper.

As shown in Table 1, the relevant engine power settings of interest here are 45 % and 40 % of load related to Ex.MEL cases: 15 % and 18 % respectively [4]. The turndown of Ex.MEL 18 % is more promising than the 15 % case in terms of lower load. However, both are improvements on the design MEL. Fig. 9 shows the relative changes in CO and NO for both Ex.MEL cases, alongside the MEL and PL. For CO and NO, they have been normalised to 18 % Ex.MEL, respectively and the temperature has been normalised to the PL local peak value.

The Ex.MEL cases generally show similar trends to the other two normal operations. Though, with local peak values of CO and NO above the others. These also apply to having the highest emissions at the outlet of the combustor. This is attributed to the higher pilot equivalence ratios shown in Table 1. Such high ratios were applied, to mainly maintain combustion stability as a considerable amount of air is being extracted. The 18 % Ex.MEL normalised temperature is observed to be lower than 15 % Ex.MEL case at the combustor outlet. It is due to the relatively lower total fuel mass flow used in absolute terms, combined with the relatively higher bypass air mass flow rate that furthers the temperature drop (from the region where the by-pass air is introduced at $x/L = 0.64$). Nonetheless, the NO is the highest due to higher peak standard deviation temperature T_{std} evaluated axially across the combustor.

Fig. 10 shows the CO and NO emissions of the Ex.MEL cases were compared and normalised to the MEL case at the combustor outlet. It indicates relatively high emissions values in the Ex.MEL cases. For the 15 % Ex. MEL, the CO is about the same as the design MEL with a value of one confirming that this case would be acceptable from a CO perspective while reducing load. Nevertheless, a high NO emission is more than twice the design MEL. The 18 % Ex.MEL case would give greater power/load reduction but offers a more pessimistic NO emission and marginally higher CO emissions. Both Ex.MEL cases produce far higher NO than the MEL due to the respective high equivalence ratio of the pilot burner. To benefit from greater load reductions for this technology, the 18 % Ex.MEL case was further improved by modifying the fuel split ratio (FSR).

Modifying the FSR changes the fuel-jet momentum and therefore affects the mixing quality. The modification of the fuel-jet momentum can heavily weigh on the pilot burner in altering the mixing quality to achieve a spatially homogenous distribution of the fuel-air mixture. The analysis in the previous work of the authors [11] shows a strong correlation between fuel-air unmixedness and temperature standard deviation, T_{std} , particularly during the initial stage of combustion, that eventually amplify the NOx emissions.

To determine the impact of change in FSR on emissions for the 18 % Ex.MEL, the FSR was varied as shown in Table 3. This covers a range from a 13 % reduction in FRS (meaning higher main and lower pilot equivalence ratios with respect to the default reference) to an 8 % increase in the FSR. The table also indicates the resulting pilot equivalence ratios, while the results of the simulations are shown in Fig. 11. In this figure, CO concentrations show local peak values at the same axial location ($x/L = 0.27$) except the -13 % case which shows a delayed local peak value at $x/L = 0.31$. The subsequent reduction of CO concentration for the -13 % case is slower than the others, thus leading to higher CO at the exit of the combustor. Despite the -13 % FSR being the leanest pilot case, the NO concentrations are also shown to have the

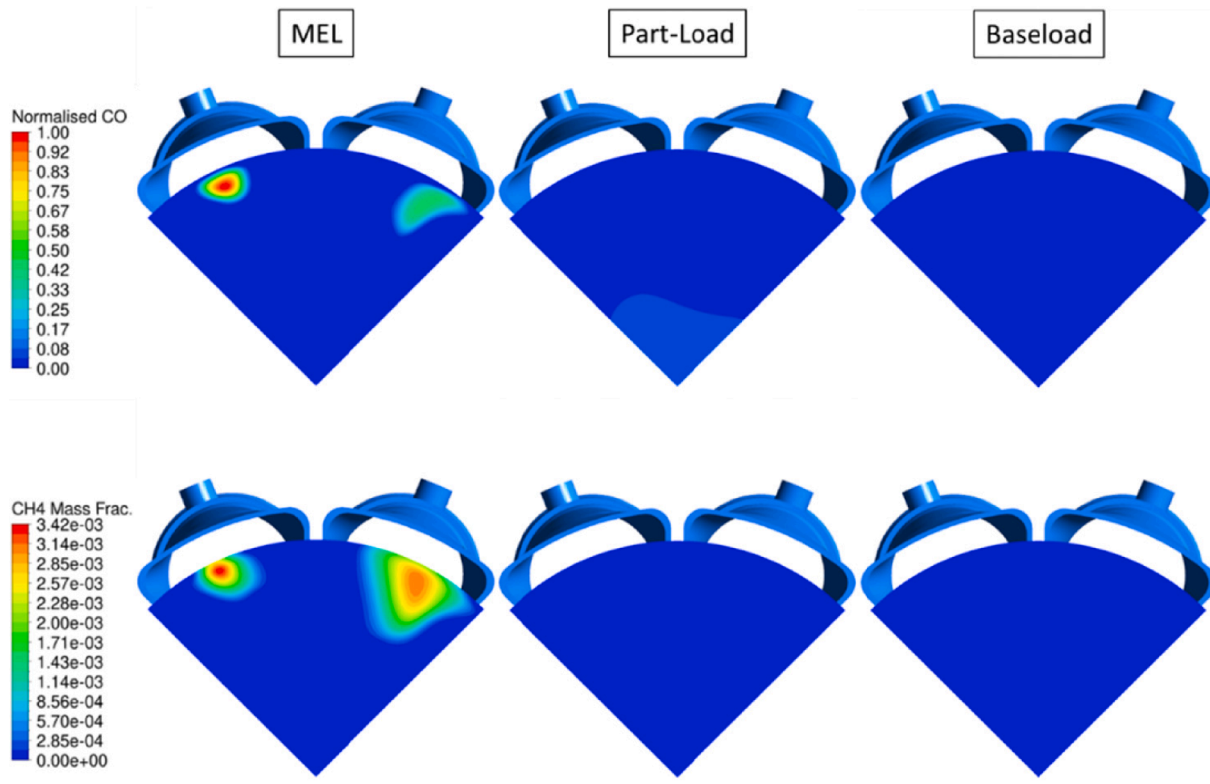


Fig. 8. Contour of normalised CO and CH₄ mass fraction for the three operating conditions at $x/L = 0.9$.

highest values throughout the combustor including the outlet. The 2 % FSR shows the lowest NO values amongst the FSR cases, throughout the combustor including the outlet. Also, from.

Fig. 12 which focuses on the emissions at the combustor outlet, it shows that its CO reduction is the most promising of the cases. In relation to the design MEL, this Ext. MEL 18 % with 2 % FSR offers a 12.3 % lower CO. The figure also shows that all directions of change in the FPR (higher and lower) can lead to higher CO NO. Though the 2 % FSR offers the best compromise, with an 18 % reduction of the NO relative to the default reference (0 % FSR); albeit at a cost of still being significantly higher than the MEL.

The Ext.EML 18 % with + 2 % FSR, being the chosen case, is compared with the MEL in terms of the structure of the flame, as shown in Fig. 13. The contour plot shows high energy densities indicated by high temperature regions, which are observed within the recirculation zone induced by the pilot burner cone. It exists in both the design and final new MEL, albeit with different intensities due to the effect of the different pilot and global equivalence ratios. The base of the flame brush, indicated by the solid black line is similar in both cases with no change in terms of the flame position of the flame root. This indicates that the flame in the Ext. EML 18 % with + 2 % FSR is also well stabilised and there is a low risk of flashback or blow-off.

6. Durability and stability analysis

Using the methodology described in subsections 3.2 and 3.3, the wall liner analysis (durability) and thermoacoustic investigation of the flame (stability) were conducted. That of the BL, PL, MEL and Ex.MEL (18 % extraction with + 2 % FSR) operations are presented here. For durability, the wall temperature distribution has been used as an indicator as shown in Fig. 14. The segments shown in this figure have been split based on that of Fig. 5. The purpose of this investigation is to determine whether the Ex.MEL brings about a greater rise in temperatures, across the wall liner, as an indicator of the impact on wall

durability. The figure shows the resulting liner wall mean temperature of each segment, showing high normalised values at segment 6. This area also coincides with areas of high gas temperature. The subsequent decreases result from cooling air from the transition pieces as shown previously. For the BL operation (the only case without the by-pass cooling), it can be observed that the peak values occur two segments downstream. More importantly, the figure shows that no unusual high temperature occurs along the liner wall for the Ex.MEL operation. The peak temperature coincides with that of the peak value of the PL operation. A dip is observed at the 11th segment in all the operations. It is due to the segment length that is relatively shorter than other segments. Hence, with the same cooling rate, the liner wall mean temperature will lower the adjacent liner wall segments. The result indicates that the Ex. MEL could be operated without any unusual penalty for the combustor durability related to temperatures.

For the thermoacoustic instability study, Table 4 shows the equivalence ratio and time delays of flames produced from the pilot and main burners for the respective operations. The flame time delay was obtained using the technique described in subsection 3.3. The first flame equivalence ratio, ϕ_1 , seems very small. This is due to the inclusion of the fuel-air mixtures inside the mixing tubes of the main burners. It is expected that this gives the correct overall temperature rise as indicated by the CFD simulation. Moreover, the local equivalence ratio may be much higher than what is shown in the table. The information shown in the table was input into the thermoacoustic code, OSCIOS. The flame equivalence ratios and the inlet pressure, temperature and air velocity were used to determine the flame thermal properties. The linear $n-\tau$ model together with flame time delays and a value of $n = 1$ was used to determine the FTF of each flame. The acoustic inlet and outlet boundary conditions have both been defined as ‘closed’ given that the compressor and turbine stages act as acoustically highly reflective boundaries.

Fig. 15 is a plot of the frequency versus the growth rate for eigenmodes determined by the thermoacoustic model. Each symbol indicates an eigenmode with frequency and growth rate as shown. The growth

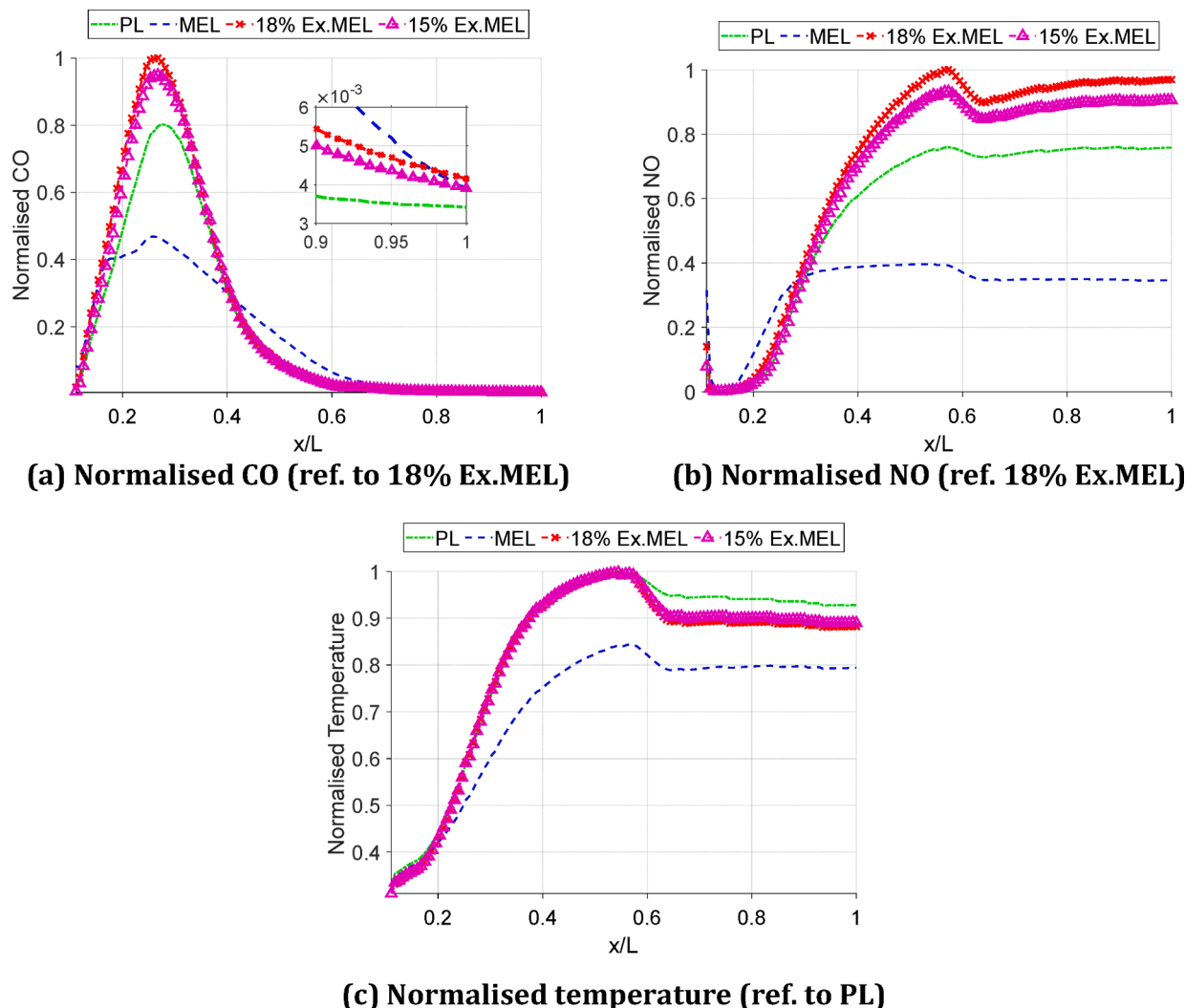


Fig. 9. Mass-average axial profiles of normalised parameters at PL, MEL and Ex.MEL cases.

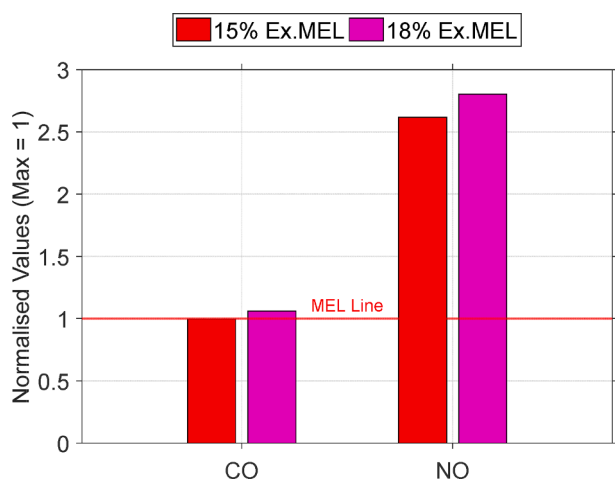


Fig. 10. Normalised CO and NO for Ext MEL cases ref. to MEL at the combustor outlet.

rate is the rate at which any random fluctuation will grow as that mode is excited. Thus, negative growth rates indicate stable modes, where any fluctuations decay away and do not lead to high amplitude pressure oscillations. Conversely, modes with a positive growth rate lead to

Table 3

Fuel split cases equivalence ratios.

Fuel Split Cases	Global equivalence ratio Φ	Pilot equivalence ratio (Φ_{pilot})
-13 %	0.47	0.65
0 %		1.65
2 %		1.78
4 %		1.91
8 %		2.15

growing fluctuations which can potentially grow to damaging levels. The horizontal dashed reference line in Fig. 15 is the frequency (270 Hz) of the main unstable mode reported by Tanaka et al. [13] for a very similar gas turbine combustor. This corresponds closely to the most unstable (highest growth rate) mode predicted (275 Hz) for the BL case and therefore supports the validity of the acoustic model. However, it is known that the combustor reported by Tanaka et al [13] can be operated with acceptable levels of thermoacoustic instabilities over a range of operating conditions due to the acoustic controls incorporated into the combustion system. The impact of additional damping due to control measures and acoustic losses (due to cooling effects) has not been incorporated into the acoustic model here. Thus, the predicted growth rates here will be higher than will occur in practice. Because of this, it is reasonable to deduce that the BL growth rate of (57/s) and frequency of

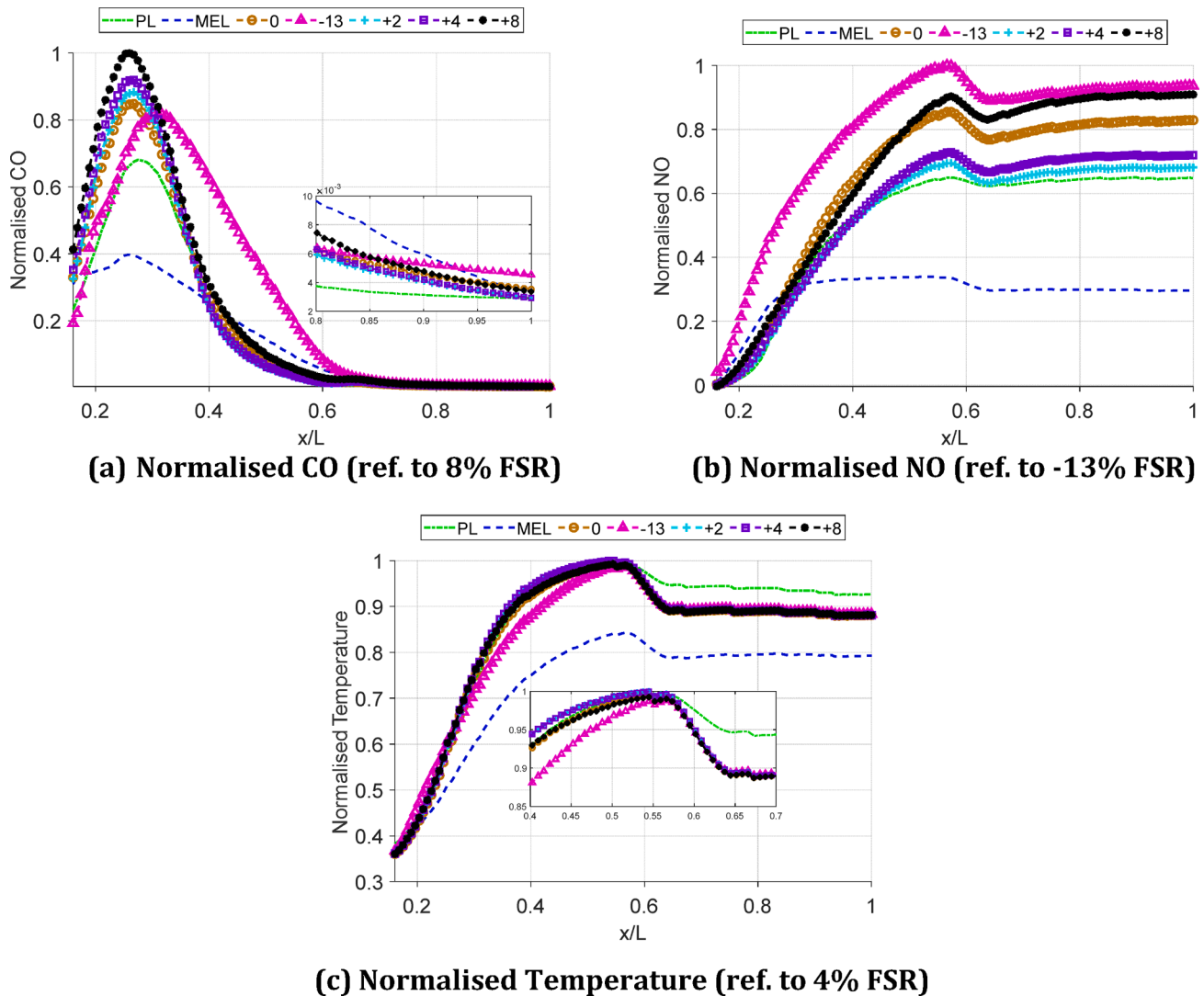


Fig. 11. Mass-average axial profiles of normalised parameters at Ext MEL 18% and FSR cases.

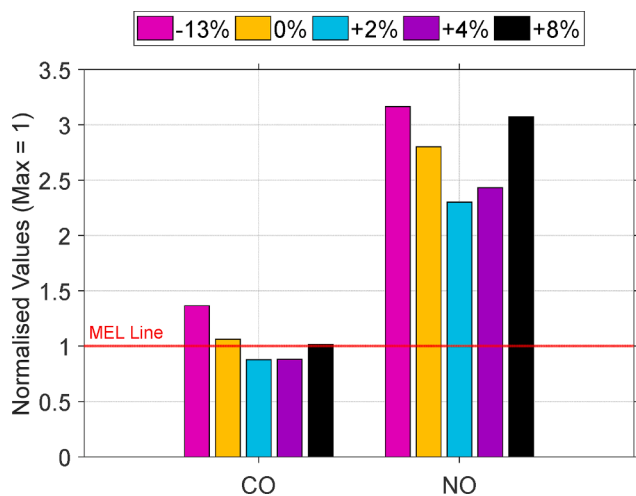


Fig. 12. Normalised CO and NO at 18% Ex.MEL with FSR cases ref. to MEL values at combustor outlet.

~ 270 Hz is an acceptable risk of oscillations at frequencies close to 270 Hz.

The most unstable mode for the MEL case is at 390 Hz with a growth rate of 8.6/s, suggesting a lower risk of high amplitude pressure oscillations than the BL case. For the PL case, the most unstable frequency is significantly higher (1431 Hz) with a growth rate of 13/s. This is below the BL growth rate, but as the frequency is significantly different, further consideration is required. The $n-\tau$ model tends to over-predict the gain of the FTF at higher frequencies because the general trend for real burners is reducing gain with increasing frequency. For example, experimental results for a given premixed burner with a gain between 0.5 and 1.5 showed a frequency up to about 200 Hz; but from 200 Hz, the gain progressively falls from 0.5 [33]. Thus, the PL mode at 1431 Hz is likely to be overpredicted and the risk of oscillations is low. This is consistent with the fact that a similar combustor operates acceptably across the load range in practice.

For the Ex.MEL case the most unstable mode is predicted to have a frequency of 1449 Hz and a growth rate of 45/s. This is a similar frequency to the PL case, but a higher growth rate. It is however lower growth rate than the BL target growth rate. However, as with the PL mode, the growth rate will likely be lower in practice due to the over-prediction of the gain at higher frequencies by the $n-\tau$ model. Additionally, it is encouraging that the predicted growth rate for the Ex.MEL case is below that of the BL case. While the Ex.MEL appears to be

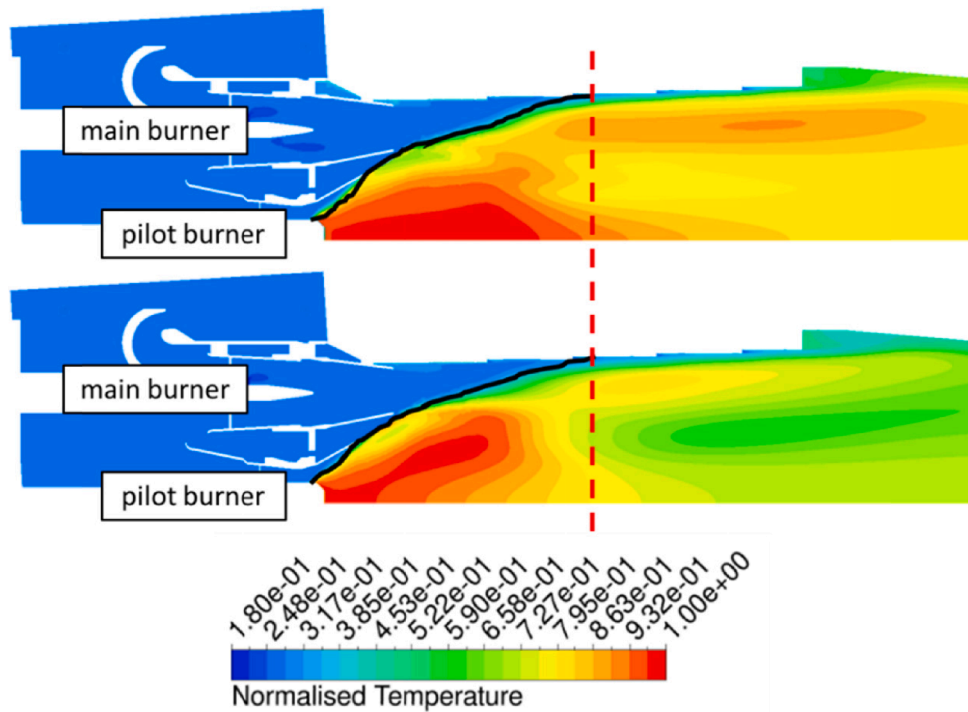


Fig. 13. Contour plot of temperature - meridional view of the MEL and Ex. EML 18 % with + 2 % FSR.

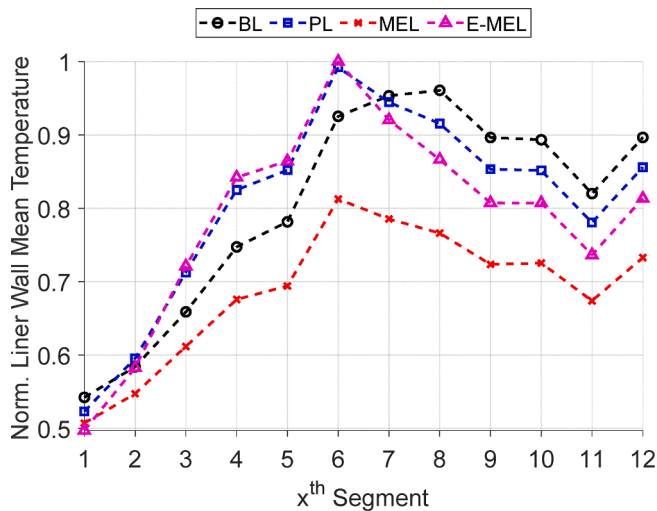


Fig. 14. Normalised liner wall mean temperature of each segment at different operations.

Table 4
Equivalence ratio and flame time delays of considered operating conditions.

Case	φ_1 [-]	τ_1 [ms]	φ_2 [-]	τ_2 [ms]
BL	0.034	2.687	0.516	5.603
PL	0.081	0.192	0.485	7.316
MEL	0.068	1.227	0.382	8.458
E-MEL	0.115	0.221	0.507	10.546

relatively safer than the BL case in this study, it is important to reiterate that thermoacoustic characteristics are likely to be more optimistic in practice when damping is incorporated.

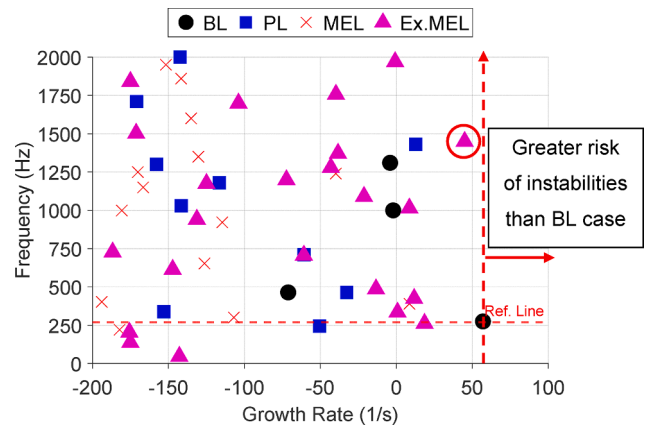


Fig. 15. Thermoacoustic instability frequencies and gains of the different operation.

7. Conclusions

Numerical calculations were carried out on a practical gas turbine combustor, to investigate the capability of extending the design MEL through high air extraction behind the last stages of the corresponding compressor. An analytical engine model and high-fidelity standalone compressor model at the same operating conditions have already been published by the authors and used to lay the foundation of the work here. These primarily provided the boundary conditions of the 3D combustor analysis in this study.

For the Design MEL case.

- As expected, MEL operation shows greater CO compared to BL and PL. This is attributed to incomplete combustion related to the low global equivalence ratio. The model adequately captures this and is evident in the fuel left over at the exit of the combustor for the MEL

case. This part of the study highlights the need to maintain or reduce CO when attaining lower load operations.

For the Ex.MEL case.

- The 18 % compressed air extraction case was found to be the best compromise between load reduction and emissions. Hence it is chosen for the MEL extension. The case provides the most reduction in load by 7 % points when benchmarked to the corresponding engine level analysis.
- An increase of the FSR by 2 % on the 18 % extraction (Ex.MEL) case brings about a reduction of the CO by 12.3 %. This shows that lower load capability can be accompanied by less CO. However, this is at the expense of a rise in NO by 130 % and 5 % in relation to the design MEL and PL (highest normal operation) respectively.
- The study highlights the challenges in identifying the optimal FSR, given that both reductions and increases in this value can exacerbate the CO and NO emissions.
- The durability analysis showed that the Ex.MEL liner temperature trends are similar to other normal operations. The local peak values observed are only minimally higher than the highest for the normal operation (PL). This is a 8.6 K higher temperature and hence not considered an operability issue.
- Most of the Ex.MEL predicted eigenmodes had negative growth rates, as shown by the thermoacoustic instabilities analysis. Only one eigenmode could be seen with a growth rate close to the reference limit, nevertheless, still lower. The predictions are likely to be more optimistic in practice, as no damping mechanism was considered.

The work has shown for the first time that the DLN combustor can handle high compressed air extraction from a compressor end, to extend the MEL to lower values, thus improve the operational flexibility of gas turbines. There is further scope for improving the fuel spit ratios, by incorporating mathematical optimisation techniques to identify where further NO reductions can be achieved without compromising on power reductions.

CRediT authorship contribution statement

Raditya Yudha Wiranegara: Formal analysis, Investigation, Methodology, Software, Validation, Visualization, Writing – original draft, Writing – review & editing. **Uyiohosa Igie:** Conceptualization, Formal analysis, Funding acquisition, Project administration, Supervision, Resources, Visualization, Writing – review & editing. **Pierre Ghali:** Formal analysis, Investigation, Methodology. **Kamal Abudu:** Resources, Validation, Writing – review & editing. **David Abbott:** Conceptualization, Formal analysis, Investigation, Supervision, Writing – review & editing. **Richard Hamilton:** Resources, Validation, Funding acquisition.

Declaration of Competing Interest

The authors declare that they have no known competing financial interests or personal relationships that could have appeared to influence the work reported in this paper.

Data availability

The data that has been used is confidential.

Acknowledgements

This work is part of the TURBO-REFLEX project that has received funding from the European Union's Horizon 2020 research and innovation programme, under grant agreement No. 764545.

Research Data Management

The author/s confirms that most of the data and methodology

supporting the findings of this study are available within the article. Further data are not publicly available due to commercial and intellectual property rights.

Appendix A. Supplementary data

Supplementary data to this article can be found online at <https://doi.org/10.1016/j.apenergy.2023.120803>.

References

- [1] P. Denholm, T. Mai, R. W. Kenyon, B. Kroposki, and M. O'Malley, "Inertia and the Power Grid: A Guide Without the Spin," Golden, CO, 2020. [Online]. Available: <https://www.nrel.gov/docs/fy20osti/73856.pdf>.
- [2] Gonzalez-Salazar MA, Kirsten T, Prchlik L. Review of the operational flexibility and emissions of gas- and coal-fired power plants in a future with growing renewables. *Renew Sustain Energy Rev* 2018;82:1497–513. <https://doi.org/10.1016/j.rser.2017.05.278>.
- [3] Abudu K, Igie U, Minervino O, Hamilton R. Gas turbine efficiency and ramp rate improvement through compressed air injection. *Proc Inst Mech Eng Part A J Power Energy Jun.* 2020;235(4):866–84. <https://doi.org/10.1177/0957650920932083>.
- [4] Abudu K, Igie U, Minervino O, Hamilton R. Gas turbine minimum environmental load extension with compressed air extraction for storage. *Appl Therm Eng Nov.* 2020;180:115869. <https://doi.org/10.1016/j.applthermaleng.2020.115869>.
- [5] T. Lecomte et al., "Best Available Techniques (BAT) Reference Documents for Large Combustion Plants," Luxembourg, 2017.
- [6] R. Kulkarni, M. Duesing, T. Ferreira-Providakis, and T. Marchione, "Large Eddy Simulation and CO Prediction of Reheat Burner Switch-Off Concept," Jun. 2015. 10.1115/GT2015-43321.
- [7] D. Therhorn, M. Gassner, V. Lonnew, M. Zhang, and S. Bernero, "CCPP Operational Flexibility Extension Below 30% Load Using Reheat Burner Switch-Off Concept," Jun. 2015. 10.1115/GT2015-42446.
- [8] F. Magni, F. Grimm, S. Sorato, and M. Micheli, "GT13E2 Low Part Load Operation: Extended Flexibility Down to 30% Load," Jun. 2016. 10.1115/GT2016-57317.
- [9] U. Igie, M. Abbondanza, A. Szymański, and T. Nikolaidis, "Impact of compressed air energy storage demands on gas turbine performance," *Proc. Inst. Mech. Eng. Part A J. Power Energy*, p. 095765092090627, Feb. 2020. 10.1177/0957650920906273.
- [10] Szymanski A, Igie U, Abudu K, Hamilton R. Aerodynamic limits of gas turbine compressor during high air offtakes for minimum load extension. *Appl Therm Eng* 2021;189:116697. <https://doi.org/10.1016/j.applthermaleng.2021.116697>.
- [11] Wiranegara RY, Igie U, Ghali P, Zhao R, Abbott D, Hamilton R. Numerical Study of Radiation and Fuel-Air Unmixedness on the Performance of a Dry Low NOx Combustor. *ASME Open J Eng Jan.* 2022;1. <https://doi.org/10.1115/1.4055983>.
- [12] Nikolaidis T. TURBOMATCH Scheme for Aero/Industrial Gas Turbine Engine. *Cranf. Univ;* 2015.
- [13] Tanaka K, Nishida K, Akizuki W. Gas turbine combustor technology contributing to environmental conservation. *Mitsubishi Heavy Ind Tech Rev* 2009;46(2):6–12.
- [14] D. Jeong and K. Y. Huh, "Numerical Simulation of Non-Reacting and Reacting Flows in a 5MW Commercial Gas Turbine Combustor." pp. 739–748, Jun. 08, 2009. 10.1115/GT2009-59987.
- [15] T. Cardoso de Souza, R. J. M. Bastiaans, B. J. Geurts, and L. P. H. De Goey, "LES and RANS of Premixed Combustion in a Gas-Turbine Like Combustor Using the Flamelet Generated Manifold Approach." pp. 1119–1127, Jun. 06, 2011. 10.1115/GT2011-46355.
- [16] J. S. Park, N. Yun, H. Moon, K. M. Kim, S.-H. Kang, and H. H. Cho, "Thermal Analysis of Cooling System in a Gas Turbine Transition Piece." pp. 1915–1924, Jun. 06, 2011. 10.1115/GT2011-45961.
- [17] Mansouri Z, Boushaki T. Experimental and numerical investigation of turbulent isothermal and reacting flows in a non-premixed swirl burner. *Int J Heat Fluid Flow* 2018;72:200–13. <https://doi.org/10.1016/j.ijheatfluidflow.2018.06.007>.
- [18] D. Pampaloni, P. C. Nassini, A. Andreini, B. Facchini, and M. Cerutti, "Numerical Investigations of Pollutant Emissions from Novel Heavy-Duty Gas Turbine Burners Operated With Natural Gas," *J. Eng. Gas Turbines Power*, vol. 142, no. 3, Feb. 2020, 10.1115/1.4045101.
- [19] Shih T-H, Liou WW, Shabbir A, Yang Z, Zhu J. A new k-ε eddy viscosity model for high Reynolds number turbulent flows. *Comput Fluids* 1995;24(3):227–38. [https://doi.org/10.1016/0045-7930\(94\)00032-T](https://doi.org/10.1016/0045-7930(94)00032-T).
- [20] Peters N. Laminar flamelet concepts in turbulent combustion. *Symp Combust Jan.* 1988;21(1):1231–50. [https://doi.org/10.1016/S0082-0784\(88\)80355-2](https://doi.org/10.1016/S0082-0784(88)80355-2).
- [21] Zimont VL. Theory of turbulent combustion of a homogeneous fuel mixture at high Reynolds numbers. *Combust Explos Shock Waves* May 1979;15(3):305–11. <https://doi.org/10.1007/BF00785062>.
- [22] Zimont V, Polifke W, Bettelini M, Weisenstein W. An Efficient Computational Model for Premixed Turbulent Combustion at High Reynolds Numbers Based on a Turbulent Flame Speed Closure. *J Eng Gas Turbines Power Jul.* 1998;120(3): 526–32. <https://doi.org/10.1115/1.2818178>.
- [23] Ruan S, Swaminathan N, Isono M, Saitoh T, Saitoh K. Simulation of Premixed Combustion with Varying Equivalence Ratio in Gas Turbine Combustor. *J Propuls Power Feb.* 2015;31(3):861–71. <https://doi.org/10.2514/1.B35517>.
- [24] Y. Liu et al., "Development and application of a preliminary design methodology for modern low emissions aero combustors," *Proc. Inst. Mech. Eng. Part A J. Power Energy*, vol. 0, no. 0, p. 095765092091954, Apr. 2020, 10.1177/0957650920919549.

- [25] P. P. Walsh and P. Fletcher, "Properties and Charts for Dry Air, Combustion Products and other Working Fluids," in *Gas Turbine Performance*, Oxford, UK: Blackwell Science Ltd, 2004, pp. 102–142. 10.1002/9780470774533.ch3.
- [26] Li, D. Yang, C. Luzzato, and A. S. Morgans, "Open Source Combustion Instability Low Order Simulator (OSCILOS-Long) Technical Report," London, UK, 2017.
- [27] Crocco L. Aspects of Combustion Stability in Liquid Propellant Rocket Motors Part I: Fundamentals. Low Frequency Instability With Monopropellants. J Am Rocket Soc Nov. 1951;21(6):163–78. <https://doi.org/10.2514/8.4393>.
- [28] Dowling AP. Nonlinear self-excited oscillations of a ducted flame. J Fluid Mech Sep. 1997;346:271–90. <https://doi.org/10.1017/S0022112097006484>.
- [29] Polifke W, Lawn C. On the low-frequency limit of flame transfer functions. Combust Flame Nov. 2007;151(3):437–51. <https://doi.org/10.1016/j.combustflame.2007.07.005>.
- [30] Lieuwen T, Torres H, Johnson C, Zinn BT. A Mechanism of Combustion Instability in Lean Premixed Gas Turbine Combustors. J Eng Gas Turbines Power Jan. 2001; 123(1):182–9. <https://doi.org/10.1115/1.1339002>.
- [31] H. Maghon, A. Kreutzer, and H. Termuehlen, "The V84 gas turbine designed for base-load and peaking duty," in *Proceedings of the American Power Conference*, 1988, pp. 218–228.
- [32] Gokulakrishnan P, et al. A Novel Low NOx Lean, Premixed, and Pre vaporized Combustion System for Liquid Fuels. J Eng Gas Turbines Power May 2008;130(5). <https://doi.org/10.1115/1.2904889>.
- [33] Han X, Li J, Morgans AS. Prediction of combustion instability limit cycle oscillations by combining flame describing function simulations with a thermoacoustic network model. Combust Flame 2015;162(10):3632–47. <https://doi.org/10.1016/j.combustflame.2015.06.020>.

2023-02-17

Minimum environmental load extension through compressed air extraction: numerical analysis of a dry low NO_x combustor

Wiranegara, Raditya Yudha

Elsevier

Wiranegara RY, Igie U, Ghali P, et al., (2023) Minimum environmental load extension through compressed air extraction: numerical analysis of a dry low NO_x combustor, *Applied Energy*, Volume 336, April 2023, Article number 120803

<https://doi.org/10.1016/j.apenergy.2023.120803>

Downloaded from Cranfield Library Services E-Repository